ELSEVIER

A statistical TEM investigation of dislocation channeling mechanism in neutron irradiated zirconium alloys

F. Onimus [a,*], I. Monnet [a], J.L. Béchade [a], C. Prioul [b], P. Pilvin [c]

[a] *Service de Recherches Métallurgiques Appliquées, CEA-Saclay, 91191 Gif-sur-Yvette, France*
[b] *Laboratoire de Mécanique des Sols, Structures et Matériaux, Ecole Centrale Paris, 92295 Châtenay-Malabry, France*
[c] *Laboratoire de Génie Mécanique et Matériaux, Université de Bretagne Sud, 56321 Lorient, France*

Abstract

Plastic deformation in irradiated zirconium alloys occurs in a very heterogeneous manner at the grain scale by the clearing up of radiation-induced prismatic loops by gliding dislocations and the channeling of these dislocations inside narrow bands of the grain. A statistical TEM investigation of this mechanism has been performed on neutron irradiated recrystallized Zr alloys tested at 350 °C. Due to the strong anisotropy of plastic deformation, different loading conditions have been investigated. It is shown that for transverse tensile tests and closed end burst tests, only basal channels are observed, whereas for axial tensile tests, prismatic and pyramidal channels are observed. This phenomenon can be understood in terms of texture and interactions between dislocations and irradiation induced loops. From Schmid factor calculations, we have also been able to prove that irradiation leads to a higher increase of critical resolved shear stresses for prismatic and pyramidal slip systems than for basal slip system.
© 2004 Elsevier B.V. All rights reserved.

PACS: 61.80.Hg; 61.16.Bg; 62.20.Fe

1. Introduction

Zirconium alloys cladding tubes containing the fuel of pressurized water reactors (PWR) nuclear power plants constitute the first barrier against the dissemination of radioactive elements. In order to improve the material and guaranty the cladding integrity even for severe in-service conditions, such as rapid power transients and during storage end of life conditions, it is necessary to develop a predictive modeling of the mechanical behavior of irradiated zirconium alloys. Lately a so-called micromechanical modeling, based on homogenization theory and deformation mechanisms, has been developed [1,2] for the non-irradiated material. This type of approach has

proved to be very successful to predict the mechanical behavior of the non-irradiated material with different textures, different chemical compositions and for different loading paths. In order to extend this type of approach to irradiated zirconium alloys, it is necessary to identify and understand, by means of an appropriate experimental approach, the key physical parameters and mechanisms that must be taken into account in the model.

It is known that from a macroscopic point of view, neutron irradiation leads to a significant increase in strength and a strong reduction in uniform elongation with an associated highly localized necking. From a microscopic point of view, it has been clearly established by an international round-robin study [3] that in zirconium alloys, radiation damage at low fluences ($\phi_t < 3 \times 10^{25}$ n/m² according to [4]) consists mainly in the formation of $\langle a \rangle$ type prismatic loops in prismatic habit planes. The increase in strength observed in different irradiated materials is usually attributed to the

---

* Corresponding author. Tel.: +33-1 69 08 44 29; fax: +33-1 69 08 71 30.

E-mail address: fabien.onimus@cea.fr (F. Onimus).

presence of the high density of small irradiation induced loops as reviewed by Bement [5] and Hirsch [6]. Indeed, according to Foreman [7], point defect clusters can act as obstacles against the glide of dislocations mainly because of contact interactions between loops and dislocations. Nevertheless these obstacles can be overcome by dislocations when a sufficient stress is applied, the loops being subsequently annihilated or dragged by dislocations following different possible mechanisms. This process of removal of irradiation loops by moving dislocations produces a cleared zone free of defects inside the grain. These obstacle-free channels or swaths will therefore constitute preferred areas for further dislocation gliding, leading to plastic strain localization at the grain scale with regions of very high local plastic strain surrounded by regions of almost zero plastic strain. This process, called dislocation channeling, has been observed in many different irradiated materials as reviewed by Wechsler [8]. In the case of zirconium alloys, several authors have reported defect free channels [9–14], however there is yet no agreement on the activated slip systems in irradiated zirconium alloys especially for various loading paths.

This paper describes TEM investigations of dislocation channeling in recrystallized zirconium alloys by means of a statistical method, considering different loading paths. Thin foils taken from specimens deformed in transverse tensile tests, closed end burst tests and axial tensile tests at 350 °C have been investigated. The results are interpreted in terms of texture and critical resolved shear stresses (CRSS). Special interest has been taken on the link between Schmid factors and the occurrence of channeling. These calculations lead to estimate the CRSS of the different slip systems. The hardening mechanisms as well as the loop annihilation mechanisms are discussed. The evolution of the volume fraction of basal channels with plastic strain is also estimated and the volume fraction of basal channels for each grain is correlated to the grain orientation.

2. Materials and experimental procedure

2.1. Materials

Mechanical tests and TEM investigations have been performed on five different specimens, A, B, C, D and E, taken from three different fully recrystallized zirconium

alloys: 'high Sn' Zy-4, 'low Sn' Zy-4 and a Zr–1%Nb–O alloy. The chemical weight composition of the three zirconium alloys used in this study are given in the Table 1.

The A and B tensile specimens have been taken in the transverse direction from two different recrystallized Zy-4 cold rolled sheets with the same chemical composition. The A specimen has been taken in a 1 mm thick sheet in the plane TD–LD whereas the B specimen has been taken in a 10 mm thick sheet in the plane TD–ND. In the case of the thick sheet (B specimen), the mean grain size was larger than in the other studied materials, typically 25 μm instead of 8 μm for usual recrystallized materials. In both cases the sheet textures are typical of rolled plates as determined by standard X-ray diffraction technique. The {0 0.2} and {1 0.0} pole figures of the thin sheet (A specimen) are given in Fig. 1(a) and (b). The A and B specimen gauges are 12.5 mm long and 2.5 mm wide. The specimens have been irradiated in the experimental reactor Siloé (CEA-Grenoble) to a neutron fluence of 0.6×10^{25} n/m² ($E > 1$ MeV) at a temperature of 280 °C.

The C and E specimens have been taken from a Zr–1%Nb–O cladding which is a first experimental grade M5 referred as M5-0 in [15]. Its microstructure is characterized by alignments of precipitates crossing the recrystallized grains parallel to the cold-rolling direction, and composed with fine β-Nb (40 nm) and some coarser β-Zr particles. The texture is typical of a fully recrystallized cladding texture as represented in Fig. 1(e) and (f). The Zr–1%Nb–O cladding has been irradiated in PWR to a neutron fluence of 12×10^{25} n/m² ($E > 1$ MeV) at a temperature of 350 °C. After irradiation, a 120 mm long section (C specimen) has been taken from the cladding and sealed at one end by means of a cold-crimped Swagelock and linked to a high pressure system at the other end in order to perform a closed end burst test. Another 60 mm long section (E specimen) has been taken from the cladding and machined in order to make a twin axial tensile specimen as shown in Fig. 2(c).

The D specimen is a section of a Zy-4 cladding. The texture is also typical of a fully recrystallized cladding as represented in Fig. 1(c) and (d). A 90 mm section of the cladding has been sealed and irradiated in the experimental reactor Osiris (CEA-Saclay) at 350 °C, to a fluence of 0.4×10^{25} n/m² ($E > 1$ MeV). Then this specimen has been linked with a high pressure system at one end in order to perform a closed end bulge test which consists

Table 1
Chemical composition of the alloys (wt%)

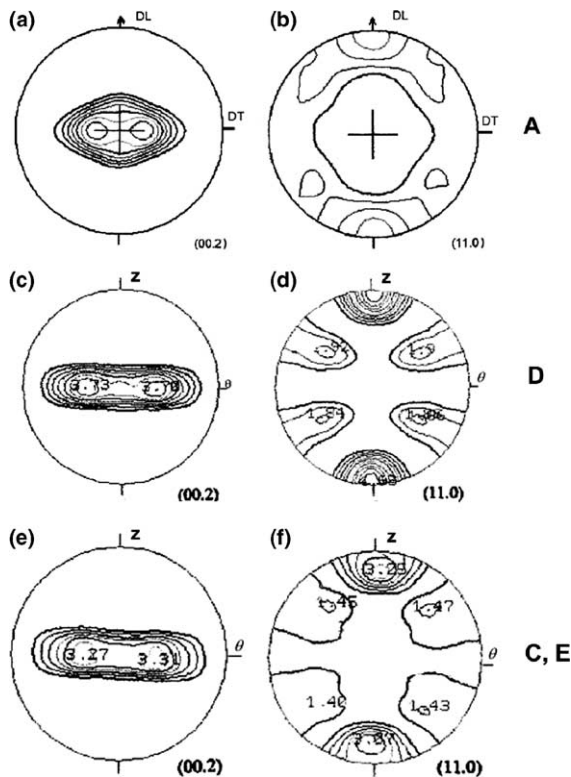| Specimen	Alloy	Sn	Fe	Cr	Nb	O	Zr
A, B	Zy-4	1.40	0.20	0.105	–	0.125	Bal.
D	Zy-4	1.30	0.210	0.10	–	0.125	Bal.
C, E	Zr–1%Nb–O	–	0.02	–	1.0	0.125	Bal.

Fig. 1. (a) {0 0.2} pole figure for the recrystallized Zy-4 cold rolled thin sheet. (b) {1 0.0} pole figure for the recrystallized Zy-4 cold rolled thin sheet (A specimen). (c) {0 0.2} pole figure for the recrystallized Zy-4 cladding (D specimen). (d) {1 0.0} pole figure for the recrystallized Zy-4 cladding (D specimen). (e) {0 0.2} pole figure for the recrystallized Zr–1%Nb–O cladding (C and E specimens). (f) {1 0.0} pole figure for the recrystallized Zr–1%Nb–O cladding (C and E specimens).

of a closed end burst test interrupted before uniform elongation. The characteristic of the materials and irradiation conditions are reported in Table 2.

2.2. Mechanical testing

On the A and B specimens transverse tensile tests have been performed at 350 °C with strain rate of 1.6×10^{-4} s^{-1}. In the case of the A specimen, the test has been interrupted before uniform elongation at a plastic strain of 0.4%. The specimen did not exhibit any shear bands or necking at the macroscopic scale. In the case of the B specimen, the test has been conducted until failure. On these two specimens, no dimensional measurements have been performed after testing.

On the C specimen a closed end burst test at a temperature of 350 °C and strain rate of 3×10^{-4} s^{-1} has been performed. A picture of the specimen after burst is reported in Fig. 2(a).

On the D specimen, a bulge test has been performed at 350 °C with strain rate of 3×10^{-4} s^{-1}. The test has been interrupted at a circumferential plastic strain of $E_{\theta\theta}^{p} = 0.2\%$. A picture of the specimen after testing is reported in Fig. 2(b).

In the case of the C and D specimens (closed end burst and bulge tests specimens), it has been possible to perform very accurate dimensional measurements via a laser imaging technique. This technique allows to measure the profile of the external diameter of the cladding after internal pressure tests with an accuracy of 2 μm.

On the E specimen, an axial tensile test has been performed. The temperature was also 350 °C and the strain rate was 3×10^{-4} s^{-1}. The test has been conducted until failure of the specimen. A picture of the specimen after failure is reported in Fig. 2(c). The plastic strain is not known accurately in this case. We therefore assume that the plastic strain far from the necking zone is close to the uniform elongation measured on the stress–strain curve which is 1.6%. The conditions of the five mechanical tests are recalled in the Table 3.
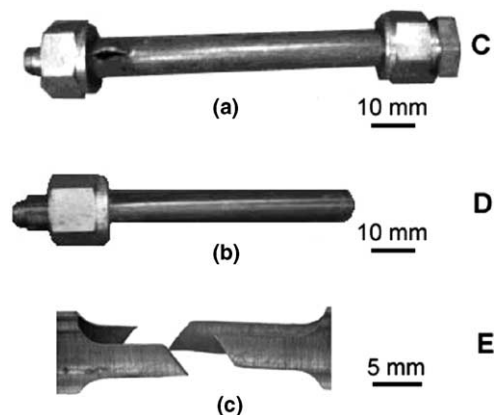

Fig. 2. C, D and E specimen after testing.

Table 2
Material and irradiation conditions of the specimens

Specimen	Material	Reactor	Fluence (n/m^2)	Irradiation temperature (°C)
A, B	Zy-4 sheet	Siloé	0.6×10^{25}	280
D	Zy-4 cladding	Osiris	0.4×10^{25}	350
C, E	Zr–1%Nb–O cladding	PWR	12×10^{25}	350

Table 3
Test conditions

Specimen	Mechanical test	Test temperature (°C)	Strain rate (s^{-1})
A, B	Transverse tensile test	350	1.6×10^{-4}
C	Closed end burst test	350	3×10^{-4}
D	Closed end bulge test	350	3×10^{-4}
E	Axial tensile test	350	3×10^{-4}

For the transverse and axial tensile tests, force and displacement were recorded. Conventional strain and stress were calculated from classical formula. For the closed end burst test, the internal pressure and the mean external diameter displacement were recorded. From this, the hoop stress $\Sigma_{\theta\theta}$ and the circumferential strain $E_{\theta\theta}$ were calculated with the usual thin wall approximation (see for instance [16]). It has to be underlined that this mechanical test leads to a biaxial stress state with $\Sigma_{zz} = \Sigma_{\theta\theta}/2$. From the stress–strain curve, we have determined conventional data such as the flow stress at 0.2% plastic strain. Furthermore, in order to have a better estimate of the true yield stress, we have decided to measure the flow stress at $0.005 \pm 0.001\%$. This measurement requires a good sensitivity of the extensometer and the optimization of the sampling frequency.

2.3. Transmission electron microscopy method (TEM)

All the thin foils were prepared in hot labs using the procedure described by Gilbon [17]. In order to relate the slip system activation to the loading conditions, a notch corresponding to the transverse direction in the case of A and B specimens and to the axial direction of the cladding in the case of C, D and E specimens has been systematically left on the thin foils and orientated parallel to the principal tilt axis of the sample holder. The TEM examinations were conducted on a Philips EM430 microscope operated at 300 kV, allowing the investigation of thick areas. Moreover, the double-tilt sample holder used in this study also permits the investigation of a relatively large angle domain ($\pm 45°$, $\pm 30°$) (the first angle corresponding to the rotation about the primary tilt axis and the second angle to the secondary tilt axis). The microstructure was studied by the conventional electron diffraction and imaging techniques. For each thin foil, we have investigated all the grains in arbitrary areas and we have determined the orientation of all the grains in this area by means of zone axis diffraction pattern indexing, leading to the drawing of the stereographic projection for each grain.

The dislocation channeling mechanism was investigated by observing the occurrence of the channels on the studied grain for the whole tilt angle domain, and by the determination of the channeling slip system. We also characterized the number of channels per grain and the channel width, leading to an estimate of the volume fraction of channels per grain.

In order to identify the channeling slip system we systematically analyzed the traces of the channels on the stereographic projection. In addition to that, the tilt conditions for the maximum contrast between channels and surrounding material, were recorded. These conditions correspond to the situation where the channeling plane contains the electron beam. These two complementary methods allow to determine the channeling slip system without ambiguity especially in the case of basal channeling. However, despite this method, few grains could contain basal channels which can not be observed, because the basal plane could not be tilted close to the electron beam considering the limitations of the double tilt sample holder, especially in the case of the A, C and D specimens. Nevertheless, in the case of the B specimen, basal channels are in very good imaging conditions for $(0°, 0°)$ tilt angles, considering the strong texture of the material. Therefore this specimen allows to confirm the results obtained from the other specimens.

3. Results

3.1. Mechanical properties and dimensional measurements

The flow stresses at 0.005% and 0.2% plastic strain for the five tests are reported in Table 4 and compared to the values obtained for non-irradiated materials. In the case of transverse tensile tests, no data was available in order to estimate the flow stress at 0.005% plastic strain. In the case of axial tensile tests, non-irradiated Zy-4 is compared to irradiated Zr–1%Nb–O.

The measurements of the profile of the external diameter of the C and D specimen, obtained by the laser imaging technique have proved that the specimens have deformed homogeneously in a large part of the gauge, as shown in Fig. 3 for the D specimen. The measured plastic deformation by the laser imaging technique in the homogeneously deformed zone of the gauge is 0.5% for the C specimen and 0.2% for the D specimen, which corresponds in the two cases to the plastic deformation measured on the stress–strain curves. Indeed, since extensometers are placed in the center of the gauge of the specimen and since in the two cases, the burst or the bulge did not appear in the center of the specimen gauge but close to the extremity of the specimen, the deformation measured by the extensometer corresponds to deformation in the homogeneously deformed zone.

Table 4
Flow stress for 0.005% and 0.2% of plastic strain for different materials and test conditions (irradiated materials compared to non-irradiated materials)

Test	Mechanical test	Material	$\Sigma_{0.005\%}$ (MPa)	$\Sigma_{0.2\%}$ (MPa)
Transverse tensile test	Non-irradiated	Zy-4	–	150
	A, irradiated	Zy-4	–	420
	B, irradiated	Zy-4	–	394
Closed end burst test	Non-irradiated	Zr–1%Nb–O	150	210
	C, irradiated	Zr–1%Nb–O	280	575
Closed end bulge test	Non-irradiated	Zy-4	150	200
	D, irradiated	Zy-4	270	540
Axial tensile test	Non-irradiated	Zy-4	100	140
	E, irradiated	Zr–1%Nb–O	350	440
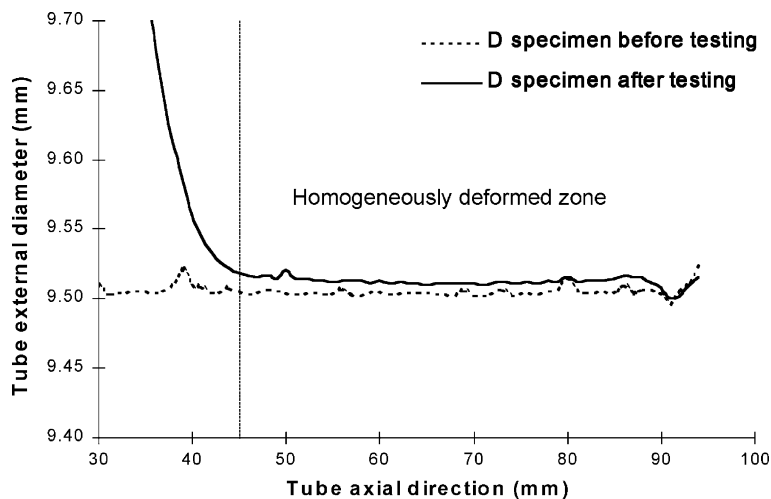
Fig. 3. Mean external diameter profile of the D specimen.

3.2. Transmission electron microscopy investigations

The as-irradiated microstructures of the five specimens used in this study are, at first order, very similar. Indeed, the main effect of irradiation, for all specimens, is the creation of a high density of point defect clusters, made of interstitials and vacancies, in the form of prismatic loops with $\langle a \rangle$ type Burgers vector in prismatic habit planes (between $\{1\,1.0\}$ and $\{1\,0.0\}$) according to Northwood [3]. The density of $\langle a \rangle$ loops is very high and similar for the five specimens. According to [18], for this irradiation temperature, the density saturation should be reached for these different neutron fluences.

The highly irradiated specimen (C and E) also showed evidence of $\langle c \rangle$ type loops which start to appear, according to [4], after neutron irradiation to around 3×10^{25} n/m^2 at this temperature.

3.2.1. Transverse tensile test specimens

The TEM observations of the thin foil taken in the gauge length of the A specimen, deformed in the transverse direction and interrupted before uniform elongation ($E^p = 0.4\%$), showed a large number of defect free channels. In this thin foil, 52 grains have been studied in different arbitrary areas. We have determined, by using the trace analysis method and the contrast criterion that 21 grains over 52 grains contained basal channels as shown in Fig. 4(a). The two stereographic projections shown in Fig. 4(b) and (c) illustrate respectively the orientation of the grain for $(0°, 0°)$ tilt angle, and the orientation of the grain corresponding to the picture in Fig. 4(a). Since for these good imaging conditions the basal plane contains the electron beam and the trace of the basal plane corresponds to the trace of the channels, the channeling plane is therefore the basal plane. No
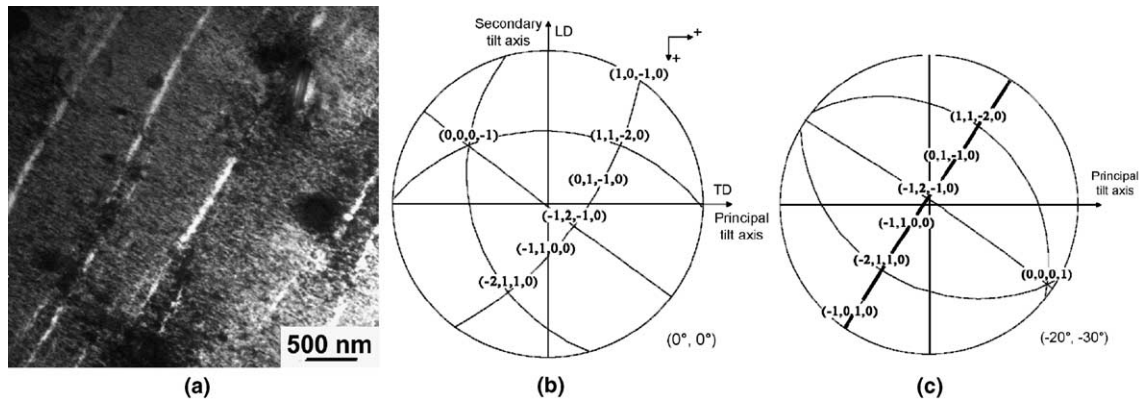
Fig. 4. (a) Basal channels observed in the A specimen, (b) stereographic projection of the studied grain corresponding to $(0°, 0°)$ tilt angles, (c) stereographic projection of the studied grain after a $(-20°, -30°)$ tilt corresponding to the orientation for the picture.

other type of channel has been observed. The number of channels per grain and the approximate width of the channels have also been investigated. These data are reported for each specimen in Table 5.

For the B specimen, machined in the thickness of the sheet (TD–ND plane), two thin foils have been taken in the gauge of the specimen far from the necking zone. According to the stress–strain plot, the recorded uniform elongation is 0.36%. The two thin foils exhibit a large number of defect free channels as in the A specimen. It has been determined that 17 grains exhibit basal channels over 29 studied grains. No prismatic nor pyramidal channel has been observed. Due to the strong texture of the material, this type of specimen is very convenient in order to investigate basal channeling. Indeed, since the specimen has been taken in the TD–ND plane, the $\langle c \rangle$ axis of the majority of the grains are contained in the plane of thin foils taken in this specimen. Therefore, the basal channels are usually in good imaging conditions for $(0°, 0°)$ tilt angles. As a consequence, in this case, there is less experimental limitation, as mentioned above, for the investigation of basal channels. An important feature which cannot be observed in the other types of thin foils taken in the other specimens is the occurrence of channels propagation to surrounding grains. For 11 grains over 17 grains with basal channels it has been shown that the channels are

linked with channels in next grains whereas in all the other specimens (A, C and D) this feature only appeared for 2 grains over 64 grains with basal channels. A picture showing basal channels propagation observed in the B specimen is reported in Fig. 5(a). The two stereographic projections shown in Fig. 5(b) and (c) correspond to the right grain in Fig. 5(a). As illustrated by the stereographic projection shown in Fig. 5(c), the channels are in good imaging conditions when the basal plane contain the electron beam, in addition the channel traces correspond to the basal plane, this implies that the channeling plane is the basal plane.

These observations are in agreement with the observations performed by Fregonese [13] and Régnard [14] who have mainly observed basal channeling in the same type of specimen. However, this study seems to be in disagreement with the observations performed by Adamson [12] for the same type of specimen (same irradiation and test conditions). Indeed, for a recrystallized Zy-2 with 1400 ppm of oxygen, Adamson only observed prismatic and pyramidal channels. These discrepancies have not yet been understood.

3.2.2. Closed end burst and bulge tests specimen

For the C specimen, two thin foils have been taken in the homogeneously plastically deformed zone ($E^p = 0.5\%$) as measured by the laser imaging technique. In

Table 5
Results of the TEM observations of the different specimens

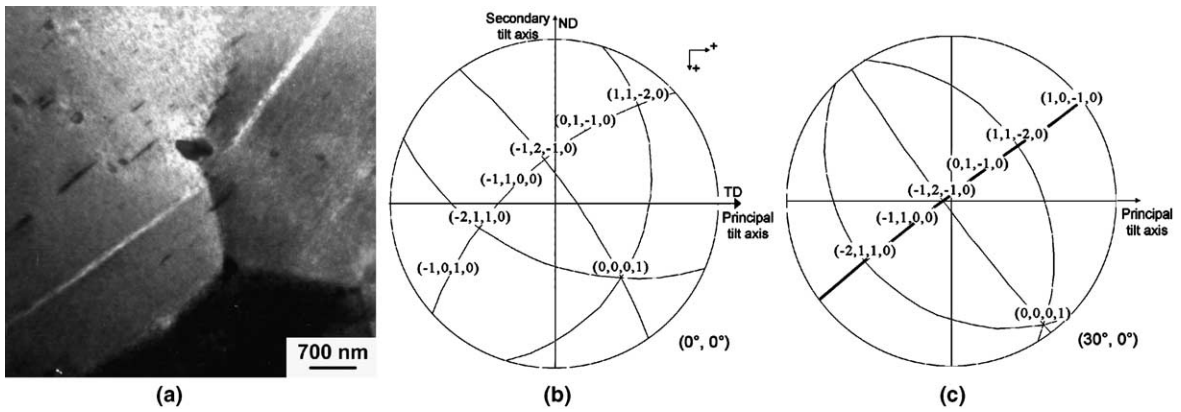| Specimen	E^p (%)	Studied grains	Grains with channels	Channeling plane	Mean number of channels	Mean width (nm)	Maximum width (nm)
A	0.4	52	21	B	3 ± 1	60 ± 10	100
B	0.36	29	17	B	5 ± 1	80 ± 40	100
C	0.5	47	28	B	4 ± 1	40 ± 20	100
D	0.2	33	15	B	3 ± 1	40 ± 20	80
E	1.6	41	20	P and π_1	5 ± 1	40 ± 20	50

Fig. 5. (a) Propagating basal channels observed in the B specimen, (b) stereographic projection of the right grain on the picture for (0°, 0°) tilt angles, (c) stereographic projection of the right grain after a (30°, 0°) tilt corresponding to the orientation for the picture.

each of these thin foils we have observed a large number of channels. The two thin foils showed the same as-deformed microstructure. It has been determined that 28 grains over 47 contained channels and all the channels were identified as basal channels as shown in Fig. 6.

For the D specimen three thin foils have been taken from the homogeneous deformation zone with 0.2% plastic strain. On overall, we have studied 33 grains. It has been determined that 15 grains over these 33 grains exhibit basal channels as shown in Fig. 7. No other type of channel was observed.

These results are in agreement with the observations performed by Pettersson [11] who also observed basal channeling for closed end burst tests at 290 °C.

3.2.3. Axial tensile test specimen

Two thin foils have been taken in the gauge length of the E specimen far enough from the necking zone. On these two thin foils, many grains containing prismatic and pyramidal channels have been observed. We have determined that 20 over 41 studied grains contain prismatic and pyramidal channels. No basal channel has been observed. As opposed to basal channels, prismatic and pyramidal channels do not seem to be fully cleared from defects and are therefore delicate to visualize. In addition to that, since the prismatic and pyramidal planes are close together, the identification of the channeling plane has been rather difficult. However, we have been able, in most cases, to distinguish between prismatic and pyramidal channels. It has been estimated that 14 grains contain prismatic channels, as shown in Fig. 8, and 4 grains contain pyramidal channels over 41 studied grains. In two cases we have not been able to distinguish between the two slip systems. The stereographic projections shown in Fig. 8(b) and (c) show that the channels are in good imaging conditions when the prismatic plane contains the electron beam which proves that the channeling plane is the prismatic plane. The
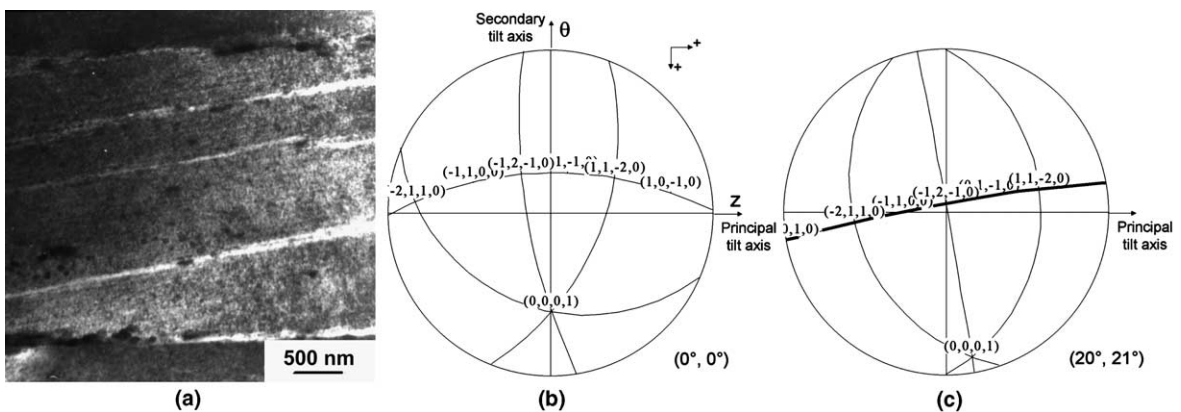

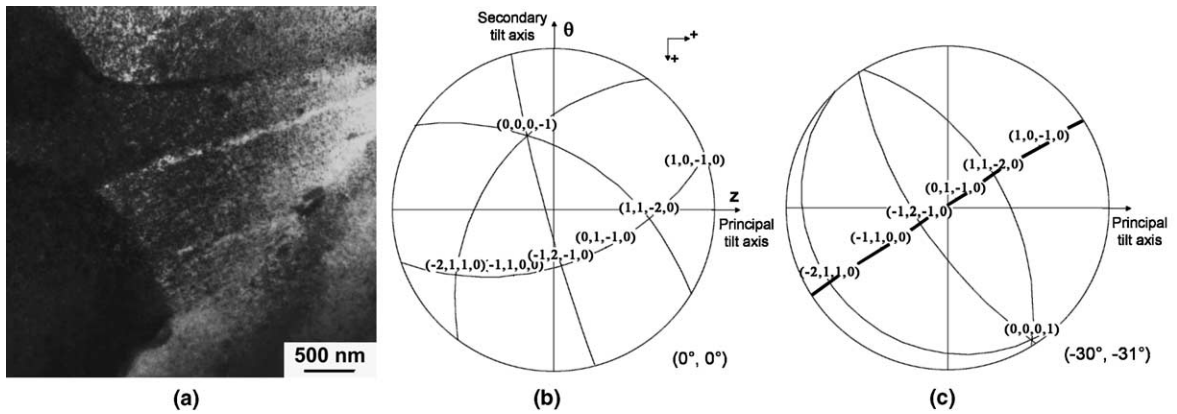Fig. 6. (a) Basal channels observed in the C specimen, (b) stereographic projection of the grain for (0°, 0°) tilt angles, (c) stereographic projection of the grain after a (20°, 21°) tilt corresponding to the orientation for the picture.

Fig. 7. (a) Basal channels observed in the D specimen, (b) stereographic projection of the grain for $(0°, 0°)$ tilt angles, (c) stereographic projection of the grain after a $(-30°, -31°)$ tilt corresponding to the orientation for the picture.
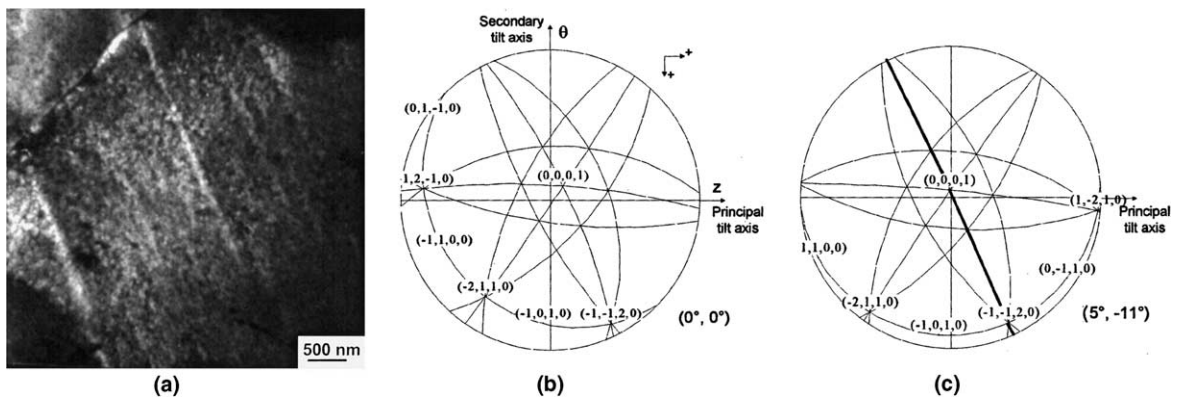

Fig. 8. (a) Prismatic channels observed in the E specimen, (b) stereographic projection of the grain for $(0°, 0°)$ tilt angles, (c) stereographic projection of the grain after a $(5°, -11°)$ tilt corresponding to the orientation for the picture.

TEM results for all the different specimens are recalled in the Table 5.

4. Discussion

The interpretation of the results obtained above will be divided in three parts. In a first part, the dimensional measurements and the TEM investigation results will be qualitatively discussed providing a coherent understanding of the plastic deformation in irradiated Zr alloys from the macroscopic and the microscopic point of views. In a second part, the calculation of the maximum Schmid factors of the different slip systems for all the studied grains will be presented and discussed. This analysis will lead to an estimation of the critical resolved shear stress (CRSS) of the different slip systems. These values will be interpreted in terms of junction reactions between dislocations and loops. Then in a third part, the

TEM results for the four specimens A, B, C and D are analyzed in terms of the volume fraction of basal channels leading to an estimate of the evolution of the volume fraction of basal channels with the plastic strain and to a correlation between the volume fraction of basal channels and the orientation of the grains.

4.1. Discussion on dimensional measurements and TEM results

The results of the accurate dimensional measurements performed on closed end bulge test specimen (Fig. 3) have shown that the circumferential plastic strain is homogeneous for the different generating lines of the cladding in one part of the specimen. This indicates that the specimen is able to deform homogeneously before reaching the maximum stress. This result is important because it has been previously discussed by Williams and Adamson [19] that the plastic deformation is probably

localized at the very beginning of the plastic flow. However, the classical dimensional measurement method used by Williams and Adamson could possibly miss very small plastic deformations typically less than $E^p = 0.5\%$. Our accurate dimensional measurements prove that a small homogeneous plastic deformation occurs before the early plastic strain localization at the specimen scale, as shear bands on tensile test specimens or as important bulging on closed end bulge test specimens. Moreover, since basal channels have been observed in the thin foils taken in the homogeneous deformation zone, it is proved that the deformation is homogeneous at the macroscopic scale although at the grain scale the deformation is localized inside the channels. The fact that, even for the interrupted test, the specimen shows some bulging could be attributed to a temperature gradient or to pre-straining due to the crimping of the Swagelocks and more generally to the high propensity of the material to localize the plastic deformation due to very small strain hardening ability. It has also to be pointed out that although some bulging can occur in one part of the specimen, the stress–strain behavior measured at the position of the extensometer still corresponds to the intrinsic behavior of the material at this position because the applied pressure is the same in all the specimen.

The measured mechanical properties indicated in Table 4 are in agreement with usual reported values. Indeed, for all loading conditions, a significant increase in strength due to irradiation is observed. The increase in yield stress due to irradiation at 5×10^{-5} plastic strain corresponds to the increase in yield stress due to the high density of radiation induced loops that must be overcome and annealed in order to produce a macroscopic plastic deformation. The increase in yield stress at 0.2% is in agreement with conventional reported data [20–22].

The TEM observations of the A, B, C and D specimen lead to the conclusion that at 350 °C, in transverse tensile tests and closed end burst or bulge tests, and for plastic strains up to uniform elongation, only basal channeling occurs. This result has to be compared with the deformation mechanisms in non-irradiated material. Indeed, it has been established, as reviewed by Douglass [23] and Tenckhoff [24], that for low plastic strains, plastic deformation occurs essentially by $\langle a \rangle$ dislocations glide in prismatic planes for axial and even transverse or closed end pressure loadings. This is due to the fact that the CRSS of the prismatic slip system is lower than that of the other slip systems. The important change in slip system activation with irradiation can be attributed to a modification in the hierarchy of the CRSS. This can be explained by the difference in the interactions between loops and dislocations which implies that dislocation channeling is easier in the basal plane than in the prismatic plane as it will be discussed later.

However, we have seen that for axial tensile tests, prismatic and pyramidal channeling occur. This is due to the fact that since the material is characterized by a strong texture with $\langle c \rangle$ axis tilted about 30° around the normal (or radial) direction in the TD–ND plane (r–θ plane), a large majority of the grains will present a very low resolved shear stress on the basal plane for axial tensile tests. Therefore, in order to accommodate plastic deformation, other slip systems, such as prismatic or pyramidal, must be activated in axial tensile loading conditions. This is in agreement with TEM investigations of thin foils taken in the E specimen.

The 3D structure of the basal channels has also been investigated thanks to the thin foils taken in the B specimen. Indeed, in the B specimen, propagation of channels from grain to grain has been observed for 11 grains over 17 with basal channels, whereas in all other specimens (A, C and D) this feature has only been observed for 2 grains over 64 with basal channels. This can be explained by the fact that the propagation of channels from grain to grain occurs in the shearing direction. In this case, since the material exhibits a strong texture ($\langle c \rangle$ axis in the ND–TD or r–θ plane), for closed end pressure test and transverse tensile test, the best orientation for the shearing direction is contained in the ND–TD plane (or r–θ plane) and tilted at 45° to the normal direction. Therefore, in order to observe channel propagation, it is necessary to take the thin foil in the ND–TD plane, as proved by TEM investigations of the B specimen. On the contrary, if the thin foil is taken in the TD–LD plane (or z–θ plane), as in the case of A, C and D specimens, the propagation of channels will be seldom observed in agreement with the TEM observations. The propagation of channels in surrounding grains is due to the high stress concentration on grain boundaries due to the strong plastic strain localization in the channel. If the surrounding grains are well oriented for basal channeling, they can accommodate the stress concentration by developing basal channeling at the position of the stress concentration which lead to channel propagation. Thus the propagation of channels should be enhanced by the strong texture of the material since many grains have the same orientation.

4.2. Schmid factor analysis

In order to compare quantitatively the change in CRSS induced by irradiation, we have computed the Schmid factor for the different slip systems of all the grains for the different loading conditions. For uniaxial tensile test the Schmid factor is classically defined as (1):

$$F_s = \frac{\tau_s}{\Sigma}. \tag{1}$$

However, in order to generalize the concept of Schmid factor for biaxial loading, we define the Schmid factor as

the resolved shear stress divided by twice the maximum shear stress associated with the biaxial stress state. In the case of closed end burst test with the thin wall approximation, the Schmid factor on the s slip system is then defined as (2):

$$F_s = \frac{\tau_s}{\Sigma_{\theta\theta}}. \tag{2}$$

The resolved shear stress is computed as (3):

$$\tau_s = \Sigma : \mu_s, \tag{3}$$

where μ_s is the orientation tensor for the slip system s defined by the normal of the slip plane n_s and by the glide direction l_s. The orientation tensor can be written in (4):

$$\mu_s = \frac{1}{2}(l_s \otimes n_s + n_s \otimes l_s). \tag{4}$$

Since for transverse tensile tests and closed end burst tests, only basal channels are observed, we have computed the maximum Schmid factor for the basal slip system, assuming that the channeling basal system corresponds to the maximum basal Schmid factor since

Burgers vector analysis for gliding dislocations is not possible. In fact several basal slip systems can be activated (two independent slip systems in the basal plane) and contribute to the creation of the channel, however only the best orientated system is considered here. Three different categories of grains have been distinguished: (1) grains containing basal channels, (2) grains without channel but with an orientation convenient for tilting so that the basal plane can contain the electron beam and (3) grains without visible channel, i.e. with an orientation unfavorable to tilt the basal plane so that it can contain the electron beam. The number of grains in these three categories is represented as a function of the Schmid factor in the histograms for the four different specimens (A, B, C, D) in Fig. 9(a)–(d) respectively. We have also computed the maximum prismatic Schmid factor for all the grains in the case of the four specimens (A, B, C, D), in order to compare it with the basal Schmid factor. The number of grains without prismatic channel (category (4)) is represented as a function of the maximum prismatic Schmid factor as histograms in Fig. 10(a)–(d) respectively. In the case of axial tensile tests (E specimen), the number of grains without basal channel
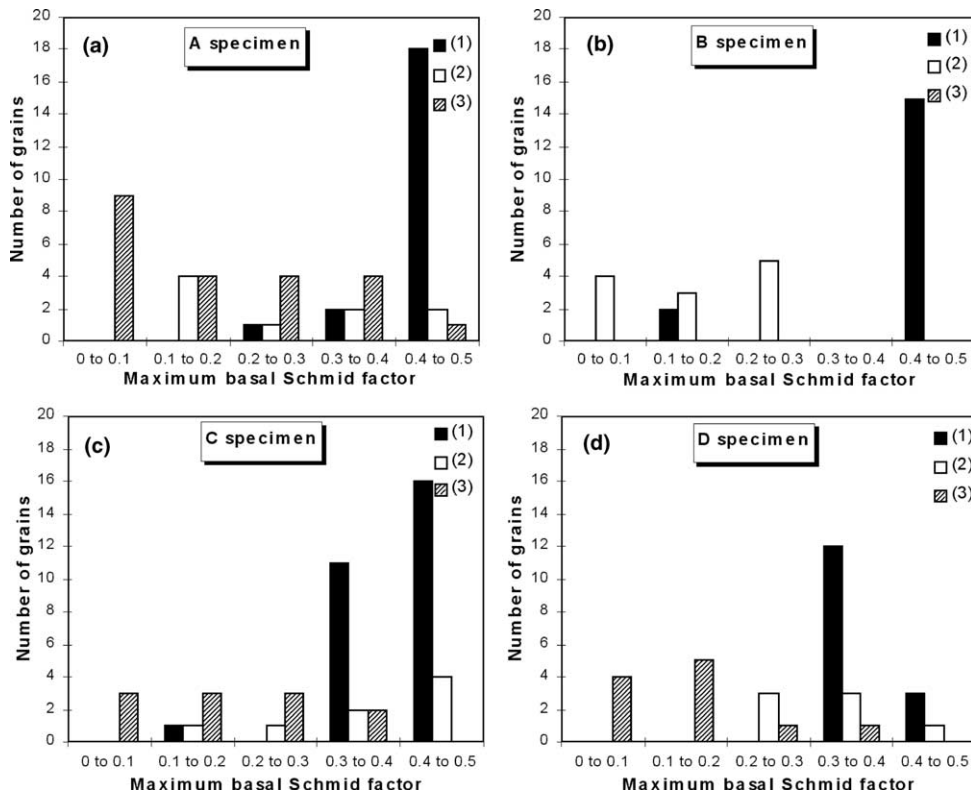

Fig. 9. Number of grains vs maximum basal Schmid factor observed in the A, B, C and D specimen ((1) grains with basal channels, (2) grains without basal channel, basal plane reachable, (3) grains without basal channel, basal plane unreachable). (a) A specimen, (b) B specimen, (c) C specimen, (d) D specimen.
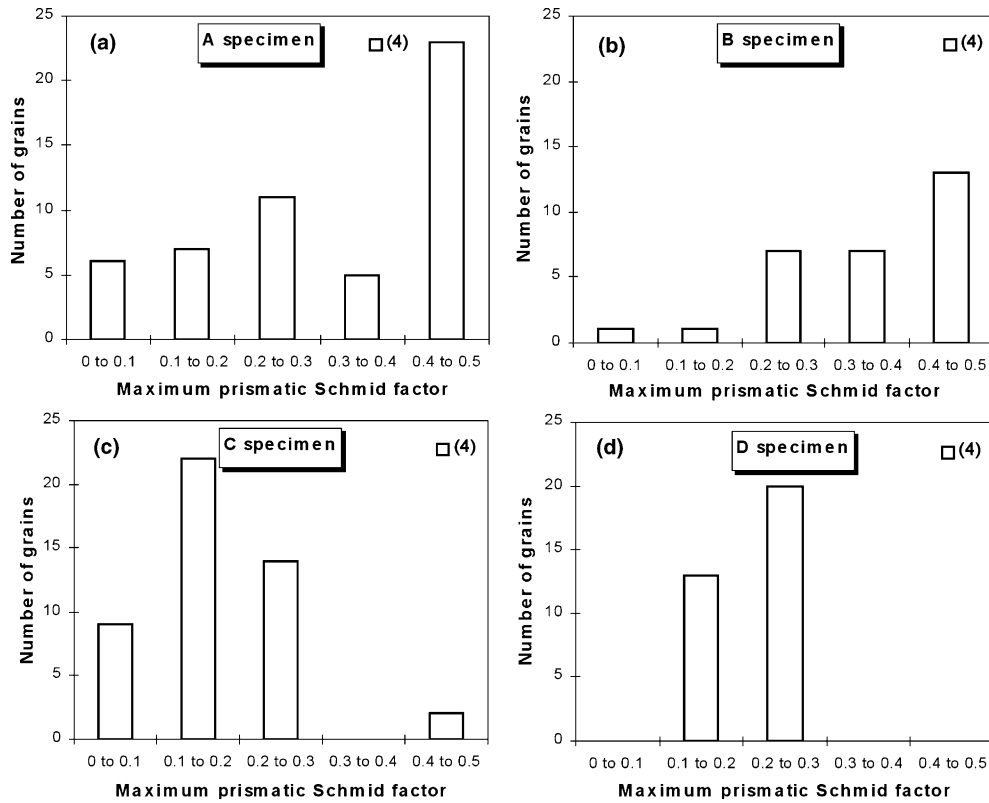
Fig. 10. Number of grains vs maximum prismatic Schmid factor observed in the A, B, C and D specimen ((4) grains without prismatic channel). (a) A specimen, (b) B specimen, (c) C specimen, (d) D specimen.

as a function of the maximum basal Schmid factor has been plotted Fig. 11(a) (category (5)). However, in the case of prismatic and pyramidal channels, the activated slip system does not often correspond to the maximum Schmid factor. This observation is surprising and does not seem to be linked with experimental artifacts. Special interaction mechanism between loops and dislocation in prismatic and pyramidal plane might explain this peculiar phenomenon. Due to this difficulty, we have chosen to plot only the number of grains containing prismatic (category (6)) and pyramidal (category (7)) channels vs the Schmid factors corresponding to the channeling plane in Fig. 11(b).

From the basal Schmid factors analysis, one can see a strong correlation between high basal Schmid factor and the occurrence of basal channeling. This confirms that channeling is linked to dislocations slip. However, the prismatic Schmid factor analysis shows that even for the grains well oriented for prismatic glide (high prismatic Schmid factor) no prismatic channels have been observed. Indeed, it has been shown that for transverse tensile tests, grains with basal Schmid factors of $F_B = 0.5$ exhibit basal channels whereas grains with prismatic Schmid factor $F_P = 0.5$ do not exhibit any prismatic

channels. This readily proves that the basal CRSS is lower than the prismatic, and pyramidal, CRSS ($\tau_B < \tau_P$ and $\tau_B < \tau_{\pi 1}$). It also confirms that, in comparison to the non-irradiated material, which only exhibits prismatic slip system activation for such a low plastic strain level, the hierarchy of CRSS has changed with irradiation.

The data given in Fig. 11(a) also prove that for axial tensile tests, the grains are not well orientated for basal slip.

From this analysis we are also able to estimate the CRSS for the different slip systems, assuming, in a first approximation, disregarding the interaction between grains, that the applied stress on each grain equals the macroscopic stress. In order to estimate the CRSS, it is necessary to estimate the true yield stress, therefore, we have chosen to compare the flow stress at 5×10^{-5} for the burst or bulge test conditions and the axial tensile test conditions. For the transverse tensile test, the mechanical test data cannot be used to estimate the flow stress at 5×10^{-5}. We have measured that for closed end burst test (C specimen), the flow stress at $E^p_{\theta\theta} = 5 \times 10^{-5}$ is $\Sigma_{\theta\theta} = 280$ MPa. We have shown from TEM examinations that, according to the histograms, well orientated grains for basal slip ($0.3 \leqslant F_B \leqslant 0.5$) exhibit basal
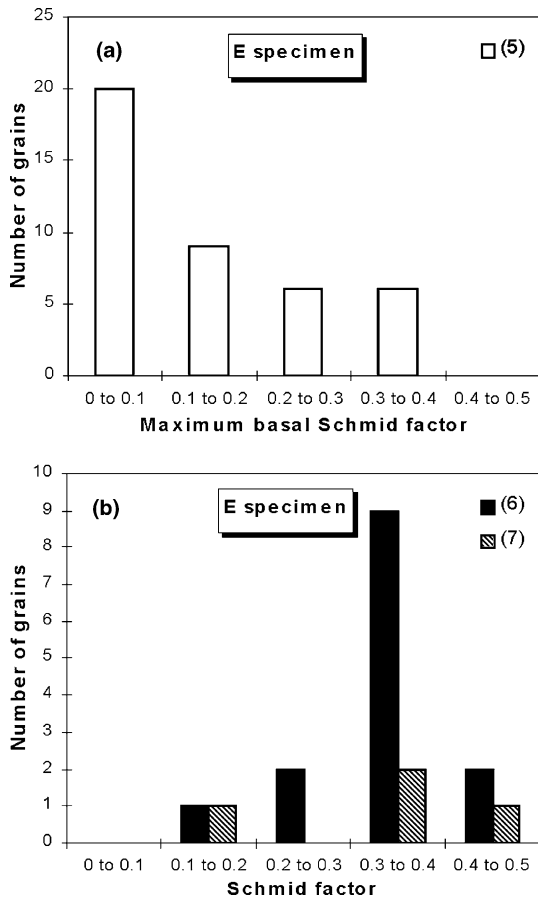
Fig. 11. (a) Number of grains vs maximum basal Schmid factor observed in the E specimen ((5) grains without basal channel, basal plane reachable), (b) Number of grains vs prismatic (6) and pyramidal (7) Schmid factor corresponding to the observed channeling plane in the E specimen.

channels, therefore, because of the definition of the Schmid factor in closed end burst tests, the CRSS of the basal plane is in between $84\ \mathrm{MPa} \leqslant \tau_B \leqslant 140\ \mathrm{MPa}$.

For axial tensile tests (E specimen) we have measured that the flow stress at $E_{zz}^p = 5 \times 10^{-5}$ is $\Sigma_{zz} = 350\ \mathrm{MPa}$. TEM observations have shown evidences that grains well orientated for prismatic slip ($0.3 \leqslant F_P \leqslant 0.5$) exhibit prismatic channels, which implies that prismatic CRSS is of the order of $105\ \mathrm{MPa} \leqslant \tau_P = 175\ \mathrm{MPa}$.

For the non-irradiated material, several authors have investigated the CRSS for single crystals α-Zr and α-Ti with different oxygen contents and for different temperatures [25,26]. All the different authors have shown that the prismatic CRSS is lower than the other CRSS. Mills [25] has shown that for zirconium single crystal with 1200 ppm oxygen concentration, the CRSS of prismatic slip system is at 350 °C of the order of $\tau_P = 40$ MPa. Conrad [26] has also reviewed the measured CRSS for prismatic and basal slip system for high purity zone

refined Ti single crystal at 350 °C. He has shown that for this temperature, the basal CRSS is twice the prismatic CRSS. Assuming the same CRSS ratio for Zr single crystal with 1200 ppm oxygen at 350 °C, the basal CRSS would be of the order of $\tau_B = 80$ MPa.

These calculations confirm that the CRSS are increased by irradiation and that the prismatic CRSS is more affected by irradiation than the basal CRSS. These phenomena can be understood in terms of obstacles to dislocation glide.

Indeed, it is known that point defect clusters, such as interstitial and vacancy $\langle a \rangle$ type loops in prismatic habit planes, can act as obstacles preventing dislocation glide, mainly because of contact interactions between loops and dislocations. The classical dispersed barrier hardening (DBH) model reviewed by Bement [5] and Hirsch [6] and numerically applied by Foreman [7] to the estimation of the CRSS of irradiated FCC materials amounts to consider that the radiation defects are randomly distributed obstacles to dislocation motion. As mentioned by Foreman, the reaction between the gliding dislocations and the intersecting prismatic loops leads to the creation of attractive junctions which can act as pinning points. In the case of zirconium alloys, the creation of junctions between $\langle a \rangle$ dislocations and $\langle a \rangle$ loops is always energetically favorable since it leads to a decrease in the Burgers vector modulus. Consider, for instance, a a_1 dislocation and a a_2 loop the junction created has a Burgers vector of $-a_3$, therefore the line tension energy of the junction is less than that of the dislocation and the loop ($a_1 + a_2 = -a_3$ and $a_3^2 < a_1^2 + a_2^2$). Nevertheless, when a sufficient shear stress is applied the obstacles can be overcome and the loops can be annihilated or dragged by the dislocations, following different mechanisms as reviewed by Wechsler [8] and Hirsch [6]. The CRSS needed to produce a macroscopic strain is obtained when the stress is sufficient to move the dislocation all across the grain. Thus, this CRSS depends on the ability of the channeling process in the slip plane. We have seen previously that the dislocation channeling mechanism is easier on the basal plane than on the prismatic plane. This can be understood, as proposed by Fregonese [13] and Régnard [14], by the fact that, in the hexagonal closed packed structure, the junctions created between a $\langle a \rangle$ loop and a $\langle a \rangle$ dislocation gliding in the basal plane are always glissile whereas in the case of a $\langle a \rangle$ dislocation gliding on the prismatic plane interacting with a $\langle a \rangle$ loop, the junction created is sessile in two cases over three, which leads to a lower ability for dislocation channeling and therefore a higher CRSS.

Indeed, let us first consider a a_1 dislocation gliding in the basal plane and interacting with a a_1 loop. In this case an helicoidal jog is created on the dislocation according to the Saada and Washburn process [6], as shown in Fig. 12(a) and (b), and the jog can glide on its

cylinder swept up by the dislocation. When a a_1 dislocation gliding in the basal plane interacts, for instance, with a a_3 loop, the junctions created have a $-a_2$ Burgers vector which is contained in the glide plane and is therefore glissile. In this case, the loop can glide on its cylinder with the junction, swept up by the dislocation as shown in Fig. 12(c) and (d). When a a_1 dislocation gliding in the prismatic plane interacts with a a_1 loop, a helicoidal jog is created on the dislocation. The jog can glide on its cylinder swept up by the dislocation (Fig. 13(a) and (b)). But in the case of a reaction between a a_1

Fig. 12. (a) and (b) Interaction between a a_1 dislocation, gliding in the basal plane, and a a_1 loop leading to the creation of an helicoidal jog which can glide on its cylinder. (c) and (d) Interaction between a a_1 dislocation, gliding in the basal plane, and a a_3 loop leading to the creation of two glissile junctions with a $-a_3$ Burgers vector allowing the loop to glide on its cylinder swept up by the gliding dislocation.

Fig. 13. (a) and (b) Interaction between a a_1 dislocation, gliding in the prismatic plane, and a a_1 loop leading to the creation of an helicoidal jog which can glide on its cylinder. (c) and (d) Interaction between a a_1 dislocation, gliding in the basal plane, and a a_3 loop leading to the creation of a sessile junction which do not lead to the sweeping up of the loop.

dislocation and a a_3 loop, the junction created has a Burgers vector $-a_2$ which is not contained in the gliding plane and is therefore sessile. Moreover, the junction is limited to a point and the glide cylinder of the loop is not well orientated for being swept up as shown in Fig. 13(c) and (d). This implies that in two cases over three the interaction is much stronger than in the case of the basal plane, leading to a lower ability for dislocation channeling process in prismatic planes as proved by the TEM analysis. This explanation also applies for pyramidal slip systems. However, when the grains are not well orientated for basal slip, as in the case of axial tensile tests, prismatic and pyramidal channeling occur in order to accommodate the plastic strain as seen by TEM investigations of the E specimen. The observation that prismatic and pyramidal channels do not seem to be fully cleared of defects could be explained by the fact that sweeping up of loops is limited for these slip systems.
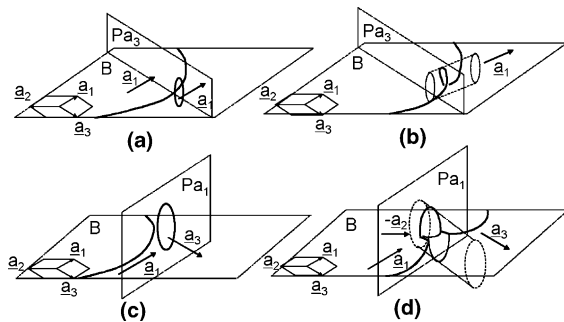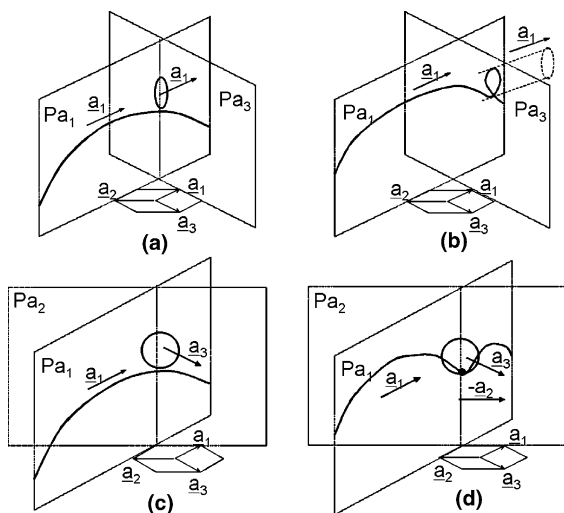
4.3. Volume fraction of basal channels

From the measurements of the number of channels per grain and the mean width of channels we have been able to roughly estimate the evolution of the mean volume fraction of basal channels with the macroscopic plastic strain (Fig. 14). The volume fraction of channels is computed as the mean width multiplied by the mean number of channels and divided by the mean grain size, 8 μm in the case of the A, C and D specimens and 25 μm in the case of the B specimen. Data reported in Fig. 14 shows that the volume fraction of channels measured on the four specimens is of the same order considering the inaccuracy of the measurements. Taking into account that there is no channel for zero plastic strain, one can
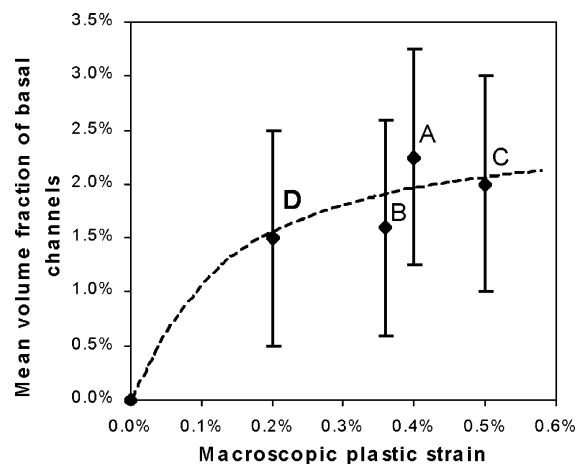

Fig. 14. Evolution of the mean basal channels volume fraction with the macroscopic plastic strain (transverse plastic strain for A and B specimens and circumferential plastic strain for C and D specimens).
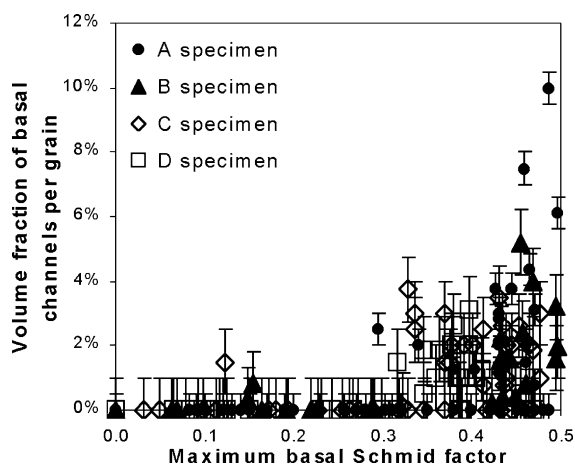
Fig. 15. Basal channel volume fraction for each studied grain of the four specimens (A, B, C, D) as a function of the maximum basal Schmid factor (transverse plastic strain for A and B specimens and circumferential plastic strain for C and D specimens).

see that there is a slow decrease in the rate of multiplication of channels. This observation is in agreement with the evolution of the number of slip bands per unit length, corresponding to the channels, with the macroscopic shear strain observed by Mori and Meshii [27] on quench-hardened aluminium single crystal surfaces.

For each grain of the four specimens (161 studied grains for the A, B, C and D specimens), the volume fraction of basal channels has also been estimated. All these data have been plotted as a function of the maximum basal Schmid factor in Fig. 15. The graph clearly shows that for a basal Schmid factor below 0.3, the volume fraction of channels is close to zero, whereas for Schmid factor between 0.3 and 0.5 the volume fraction of channels is generally less than 4% and on average of the order of 2% for all the studied grains. These statistical data can be used as an input into a micromechanical modeling of the mechanical behavior of neutron irradiated Zr alloys.

5. Conclusions

It has been shown, that, for various loading paths, dislocation channeling occurs during plastic deformation at 350 °C in neutron irradiated recrystallized zirconium alloys. It has also been proved that although plastic deformation occurs at the grain scale in a highly localized manner, it is still homogeneous at the specimen scale. A great improvement from previous works comes from the statistical TEM investigation of dislocation channeling mechanism. This investigation has shown that for transverse tensile and closed end burst tests at 350 °C, only basal channeling occurs in the homoge-

neously deformed part of the specimen. Nevertheless, due to the strong texture of the material, both prismatic and pyramidal channeling occur for axial tensile tests. These observations lead to the conclusion that irradiation induces a change in slip system activation associated with a change in the hierarchy of CRSS ($\tau_B < \tau_P$). The change of CRSS has been quantified by a statistical Schmid factor analysis. The measurement of the flow stress for 0.005% plastic strain has been used in order to estimate the basal and prismatic CRSS (105 MPa $\leqslant \tau_P \leqslant$ 175 MPa and 84 MPa $\leqslant \tau_B \leqslant$ 140 MPa in addition to the hierarchy $\tau_B < \tau_P$). The change in CRSS has been interpreted in terms of junction reactions between loops and dislocations. This analysis also holds for pyramidal (π_1) slip systems. The statistical TEM observations have also been analyzed in terms of volume fraction of basal channels. It has been shown that for Schmid factors below 0.3, the volume fraction of channels is close to zero, whereas for Schmid factors between 0.3 and 0.5 the volume fraction of channels is on average of the order of 2%.

References

[1] P. Geyer, X. Feaugas, P. Pilvin, Modeling of the anisotropic viscoplastic behavior of fully annealed zircaloy-4 tubes by a polycrystalline approach, Plasticity'99, Cancun, January 1999.
[2] R. Brenner, J.L. Béchade, O. Castelnau, B. Bacroix, J. Nucl. Mater. 305 (2002) 175.
[3] D.O. Northwood, R.W. Gilbert, L.E. Bahen, P.M. Kelly, R.G. Blake, A. Jostsons, P.K. Madden, D. Faulkner, W. Bell, R.B. Adamson, J. Nucl. Mater. 79 (1979) 379.
[4] C. Lemaignan, A.T. Motta, in: R.W. Cahn, P. Haasen, E.J. Kramer (Eds.), Nuclear Materials, in: B.R.T. Frost (Ed.), Materials Science and Technology Series, vol. 10B, VCH, New York, 1994, p. 1.
[5] A.L. Bement, in: Second International Conference on the Strength of Metals and Alloys, vol. 2, ASM, Metals Park, 1970, p. 693.
[6] P.B. Hirsch, in: Proceedings of a Conference on Point Defect Behavior and Diffusional Processes, University of Bristol, 13–16 September 1976.
[7] A.J.E. Foreman, Philos. Mag. 17 (1968) 353.
[8] M.S. Wechsler, Dislocation channeling in irradiated and quenched metals, The inhomogeneity of plastic deformation, ASM, Metals Park, Ohio, 1973, p. 19.

[9] C.E. Coleman, D. Mills, J. van der Kuur, Can. Metall. Quater. 11 (1972) 91.

[10] T. Onchi, H. Kayano, Y. Higashiguchi, J. Nucl. Mater. 88 (1980) 226.

[11] K. Pettersson, J. Nucl. Mater. 105 (1982) 341.

[12] R.B. Adamson, W.L. Bell, International Symposiums, vol. 1, Xian, China, 1985, p. 237.

[13] M. Fregonese, C. Régnard, L. Rouillon, T. Magnin, F. Lefebvre, C. Lemaignan, Zirconium in Nuclear Industry: Twelfth International Symposium, ASTM STP 1354 (2000) 377.

[14] C. Régnard, B. Verhaeghe, F. Lefebvre-Joud, C. Lemaignan, Zirconium in the Nuclear Industry, 13th International Symposium, ASTM STP 1423 (2002) 384.

[15] D. Gilbon, A. Soniak, S. Doriot, J.-P. Mardon, Zirconium in Nuclear Industry: Twelfth International Symposium, ASTM STP 1354 (2000) 51.

[16] F. Ferrer, A. Barbu, T. Bretheau, J. Crépin, F. Willaime, D. Charquet, Zirconium in Nuclear Industry, Thirteenth Symposium, ASTM STP 1423 (2002) 863.

[17] D. Gilbon, C. Simonot, Zirconium in the Nuclear Industry: Tenth International Symposium, ASTM STP 1245 (1994) 521.

[18] D.O. Northwood, Atomic Energy Review 15 (4) (1977) 547.

[19] C.D. Williams, R.B. Adamson, K.D. Olhausen, European Conference on Irradiation Behavior of Fuel Cladding and Core Component Materials, Karlsruhe, 1974, p. 189.

[20] H.R. Higgy, F.H. Hammad, J. Nucl. Mater. 44 (1972) 215.

[21] C.J. Baroch, ASTM STP 570 (1975) 129.

[22] T. Yasuda, M. Nakatsuka, K. Yamashita, Zirconium in the Nuclear Industry: 7th International Symposium, ASTM STP 939 (1987) 734.

[23] D.L. Douglass, The metallurgy of zirconium, Atomic energy review supplement, International atomic energy agency, 1971, p. 41.

[24] E. Tenckhoff, ASTM STP 966 (1988) 1.

[25] D. Mills, G.B. Craig, Trans. Metall. Soc. AIME 242 (1968) 1881.

[26] H. Conrad, Prog. Mater. Sci. 26 (1981) 123.

[27] T. Mori, M. Meshii, Acta Met. 17 (1969) 167.